Research Article Vol. 13, No. 5 / May 2026 / Optica 959

Ptychographic imaging ellipsometry with extreme ultraviolet light

Matthias Gouder,[1,2] Fengling Zhang,[1,2] Tunç Çiftçi,[1] Lars Loetgering,[3] Kjeld S. E. Eikema,[1,2] and Stefan Witte[1,4,*]

[1]Advanced Research Center for Nanolithography, Science Park 106, 1098 XG Amsterdam, The Netherlands
[2]Department of Physics and Astronomy, Vrije Universiteit Amsterdam, De Boelelaan 1081, 1081 HV Amsterdam, The Netherlands
[3]Carl Zeiss AG, Carl-Zeiss-Promenade 10, Jena 07745, Germany
[4]Imaging Physics, Faculty of Applied Sciences, Technische Universiteit Delft, Lorentzweg 1, 2628 CJ Delft, The Netherlands
*s.m.witte@tudelft.nl

Received 4 March 2026; revised 24 April 2026; accepted 24 April 2026; published 18 May 2026

Quantitative optical imaging is an important diagnostic tool for metrology and materials science. Especially in the extreme ultraviolet wavelength range, the combination of high spatial resolution and sensitivity to material properties holds promise for quantitative characterization of complex nanostructures. Unlocking this potential requires an approach that links the relevant material properties to optically measurable observables in a spatially resolved way. Here we show that high-resolution maps of the complex refractive index of a multi-element nanostructure can be reconstructed from polarization-resolved extreme ultraviolet ptychography measurements. We record ptychography data in a reflection geometry for two incident polarization states and variable angle of incidence, and show that the resulting amplitude and phase information can be analysed to yield accurate maps of the local refractive index and surface profile, using an automatic-differentiation-based reconstruction framework. Our approach enables determination of local material composition through a segmentation analysis, as well as high-resolution quantitative imaging of optically addressable properties of nanostructures.

https://doi.org/10.1364/OPTICA.596484

1. INTRODUCTION

Optical imaging is an essential diagnostic method in many areas of science, ranging from biology to materials science and semiconductor device physics. While imaging itself is relevant mainly in situations where the spatial structure of the specimen is not known a priori, or to track dynamics, in many application areas the main objective is to retrieve information about the specimen in a spatially resolved way. Examples of such quantitative imaging include the determination of degree of magnetization in metal films, ion concentrations in cells, local temperature measurements, and more (see, e.g., [1–3]). In these cases, an additional analysis step is needed that links an optically measurable quantity to the material property of interest. An essential aspect of such measurements is to retain the high spatial resolution of the imaging system, as measurement methods that can only determine spatially averaged bulk properties typically fail to capture the spatial complexity of nanostructured objects.

A general example of a material property that links to optical properties is the (complex) refractive index, usually defined as $\mathbf{n} = n + ik$. The real part n relates to the speed of light in a material, while the imaginary part describes absorption. The ability to measure refractive indices is relevant in the characterization of optical components, coatings, and thin films, and enables identification of materials if their properties are known. The standard approach to refractive index measurements is ellipsometry, which is based on measurements of the reflected optical intensity for different (usually s and p) polarization states of light, typically as a function of incident angle [4–7]. For a given polarization state and incident angle, the reflectivity of a material can be linked to the refractive index through the Fresnel equations. As these Fresnel equations generally do not have a direct inverse, a fitting procedure is used to retrieve refractive index information from the measured polarization- and angle-resolved reflectivity data. In addition to such intensity-based measurements, interferometric variations of ellipsometry have also been developed, which make use of the fact that the phase of the reflected light is also sensitive to the refractive index [8–11], albeit at the cost of increased stability requirements. Ellipsometry systems have been developed using light at wavelengths ranging from infrared to ultraviolet, and even extreme ultraviolet (EUV) implementations have been shown [12,13]. Such EUV measurements are particularly relevant for the characterization of structures that are not transparent to visible light, such as metal-containing nanostructures, and especially also semiconductor devices and integrated circuits [14–17]. The polarization

sensitivity enables more detailed analysis of material composition and refractive index than angle-resolved reflectometry [18–21].

Ellipsometry is typically performed as a point measurement method that does not provide spatially resolved information, using a relatively large and collimated beam to probe a sample [5,22,23]. It is also possible to combine ellipsometry with a spatially resolved detection system to obtain images of refractive index distributions across a sample of interest. Various implementations of such an imaging ellipsometry concept have been developed, using point-scanning [24–26] as well as wide-field [27] imaging. At EUV wavelengths, imaging ellipsometry could leverage the better diffraction limit and penetration depth into metal films, and in principle enable high-resolution quantitative imaging of complex nanostructures such as integrated circuits. However, both EUV imaging and polarization control are challenging by themselves given the limitations of EUV optics [12,28,29]. Interferometric methods at EUV wavelengths are possible for thin transmissive samples using special common path arrangements [30,31], but particularly challenging in a reflection geometry. Therefore, EUV ellipsometry has remained limited to point measurements with low spatial resolution.

To mitigate the limitations of EUV optics and enable high-resolution EUV imaging, lensless imaging methods based on coherent diffraction have been developed. Ptychography has emerged as a particularly powerful lensless EUV imaging modality, enabling near-wavelength-scale resolution and high versatility [32–35]. Furthermore, ptychography enables quantitatively accurate amplitude and phase retrieval, thanks to its ability to separate the probe field from the object reconstruction [16,36–38]. As ptychography does not require interferometric detection, it can be applied in a reflection geometry as well [39–41]. Ptychography has enabled first demonstrations of quantitative EUV imaging based on reflectometry [15,42] and scattering quotient [17]. However, ellipsometry has remained elusive, as it requires polarization-resolved measurements, and especially highly accurate relative comparisons between sequentially measured images. As ptychography only provides relative phases within an image, comparing phase measurements from separate images is not directly possible.

In this paper, we present a ptychography-based approach to imaging ellipsometry, which makes effective use of the accurate relative amplitude and phase information contained in individual ptychography reconstructions. By performing measurements in a reflection geometry for incident radiation at both s- and p-polarization, we retrieve quantitative complex reflectivity maps of a substrate-based nanostructured film containing multiple elements and height variations. The standard data analysis approach in imaging ellipsometry is to take polarization- and angle-dependent data from a single point on the object as the input to a reconstruction model, processing all object pixels independently. Instead, we take a combined reconstruction approach that specifically uses different pixels within a single image to retrieve refractive index data from multiple positions in parallel. This approach allows us to define a set of constraints based on the more accurately measured relative amplitude and phase ratios within single images. Through this approach, we obtain sufficient measurement parameters to uniquely retrieve the complex refractive index at both those object locations. We solve the resulting inverse problem by minimizing the associated complex multi-parameter loss function using an algorithm based on automatic differentiation [43].

Depending on the application, we can approach the analysis in different ways. If the main interest is in retrieving high-resolution spatial maps of local refractive index and surface profile, the analysis can be performed for each image pixel (or binned subset of pixels) independently. Alternatively, in applications where it is known that a limited number of materials and/or surface height steps are present, a segmentation analysis can be used to classify areas with identical properties, and an averaged value of material properties from those areas can be determined. We show both procedures applied to our experimental data. Our results show the potential of using ptychography for quantitative imaging, and the combination with image-based analysis enables metrology on multi-element reflective structures without a priori knowledge of the material properties. As such, it provides a combination of ellipsometry and imaging that combines the features of each modality, rather than a parallelized set of single-point ellipsometry measurements. Also similar to ellipsometry, in case of a stack of multiple partially reflective layers, a solution for the refractive index of each layer can be determined if the nominal layer structure is known.

2. MATERIALS AND METHODS

A. Experimental Setup

A ptychographic imaging ellipsometry setup requires a reflection geometry with controlled reflection angles, and the ability to record ptychography scans with orthogonal polarization states. A schematic of our instrument is shown in Fig. 1. We obtain coherent EUV radiation via high-harmonic generation (HHG) in an Argon gas jet with a backing pressure of 4 bar. The HHG is driven by 2 mJ laser pulses at a 1030 nm central wavelength and a 1 kHz repetition rate (Light Conversion Pharos) that are post-compressed to a 37 fs duration in a CASCADE-type system and focused with an $f = 30$ cm singlet lens [44]. As the HHG radiation inherits the linear polarization state of the driving laser [45], we control the polarization of the EUV radiation at the sample by tuning the drive laser polarization state with a $\frac{\lambda}{2}$-plate and avoiding polarization-sensitive components downstream. The generated harmonics are separated from the fundamental beam using a 200 nm thick Al filter. A pair of multilayer mirrors (OptixFab GmbH) in a z-configuration at 5 degree angle of incidence focuses the beam onto the sample, and simultaneously acts as a wavelength filter for the 27th harmonic at 38 nm through its optimized reflectivity curves. This focusing approach does not affect the polarization state, and through calibration measurements, we confirm that the flux on the sample does not significantly change with EUV polarization (see Supplement 1, Section 4). While the refractive index retrieval algorithm is in principle not limited to monochromatic ptychographic reconstructions, it is more challenging to get the same quantitative accuracy from a multi-wavelength ptychography measurement.

The sample is mounted on a 2D-translation stage for ptychography scans, which is placed onto an additional rotational stage for control over the reflection angle, covering a range of illumination angles from $45° \leq \theta \leq 90°$ (where 90° means having the surface parallel to the beam). Diffraction patterns are recorded on an EUV-sensitive CMOS camera (Marana-X 4.2B-11), which can be rotated around the sample via a custom-built adjustable flange mount. The pressure inside the imaging chamber is maintained in the 10^{-6} mbar range. We performed experiments on a sample containing microstructures that are lithographically etched in a silicon substrate, and subsequently covered by chromium (Cr) and gold (Au) at different locations and with different layer thickness.

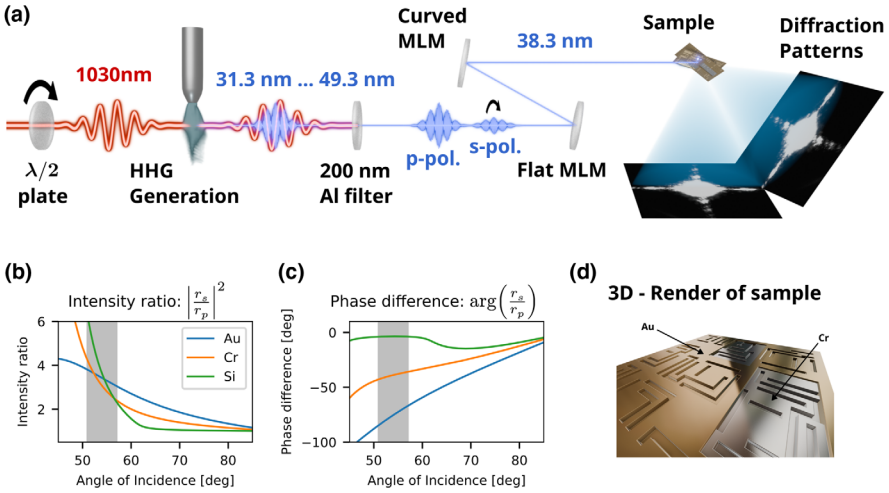

Fig. 1. Experimental setup. (a) Schematic overview of the setup. Driving laser 1030 nm (in red) is focused into an Argon gas jet, where high-harmonics are generated (in blue). The driving laser is blocked by a 200 nm aluminum filter. From all the harmonics, only $\lambda = 38$ nm is focused onto the sample by using two multilayered mirrors. The reflected field propagates to the camera where it forms diffraction patterns. The illumination angle of the sample and the polarization state of the driving laser are changed between measurements. (b, c) Amplitude ratio and phase-difference of gold (Au), chromium (Cr) and silicon (Si) when changing polarization state from linear s- to p-polarized in a range from 45° to 85° angle of incidence. The range of angles used in measurements for this work is highlighted in gray. The phase difference shown in (c) is directly derived from the Fresnel equations and does not include additional phase shifts caused by differences in heights. (d) 3D artist impression of the sample. Different colors depict different materials. Various height changes within each material are visible.

These elements show distinct amplitude and phase changes upon reflection. Our approach to retrieving complex refractive indices does not depend on absolute reflectivities, but on relative amplitude and phase changes of the electric field upon reflection for different polarization states, which are plotted in Figs. 1(b), 1(c). For a complete ptychographic ellipsometry experiment, we perform ptychography scans for s- and p-polarization sequentially, for a range of different illumination angles. Complex object reflectivity maps for both polarization states $O_{s,p}$ are then reconstructed from the recorded diffraction data using a ptychography algorithm employing automatic differentiation (see Supplement 1, Section 1).

B. Sample Fabrication

The base of the sample that we used is a Si-substrate patterned with a variety of different spatial structures. Specifically, small (2 μm) circuit-like structures are already etched 75 nm deep into the substrate. To add different elements, we first deposit a 35 nm layer of chromium Cr onto the substrate using electron beam physical vapor deposition (EBPVD). Via laser lithography using negative photoresist maN1410, we subsequently deposit a 34 nm gold Au-layer on specific parts of the sample. Through this procedure, the majority of the structures have a gold top layer, except for a set of rectangular areas where the topmost layer only contains chromium, as depicted in Fig. 1(d). More information about sample fabrication can be found in Supplement 1, Section 7.

3. RESULTS

A. Ptychographic EUV Imaging and Refractive Index Determination

In ptychography, measured diffraction patterns are modeled as an exit surface wave that has propagated to the detector. This exit surface wave is the light field directly after reflection, and consists of the product $P \cdot O$ of the incident probe field P and the complex object reflectivity map O. By measuring multiple diffraction patterns for a set of in-plane object displacements, a dataset is generated from which both P and O can be reconstructed [36,37]. This ability to separately reconstruct the probe field is a major advantage of ptychography, as it removes any influence of the illumination on the reconstructed object image, and is an important factor in the quantitative accuracy of the amplitude and phase maps. Details on our reconstruction procedure are given in Supplement 1, Sections 1 and 2. At this point, we should note two important aspects about ptychography that complicate any analysis that requires multiple independent image reconstructions. First, phase images of P and O are recovered up to an unknown constant, so it is not directly possible to compare absolute phase values from independent measurements. Second, as the measurement is only sensitive to $P \cdot O$, comparing object amplitudes from independent measurements is only possible by normalizing the probe amplitudes. Figure 2(a) shows a typical ptychography reconstruction from a dataset recorded at an incident angle of $\theta = 51°$ with respect to the surface plane and s-polarized EUV radiation. The phase variations between different structures are accurately retrieved through the reconstruction algorithm. Height variations and changes in material composition are clearly observable as phase shifts in the images. As an independent reference of the height variations, we perform atomic force microscopy (AFM) measurements on the object. Figure 2(b) shows an image of the same surface area, with a lineout across the various height steps displayed in Fig. 2(c). The rectangular features visualize the presence of pure Cr, without an additional Au-layer.

To reconstruct refractive index data from a ptychography dataset, further analysis steps are needed. From the discussion above, it is clear that the retrieved object O contains the complex reflectivity of the sample, but with a possible amplitude scaling and a global phase offset. In general, the complex reflectivities

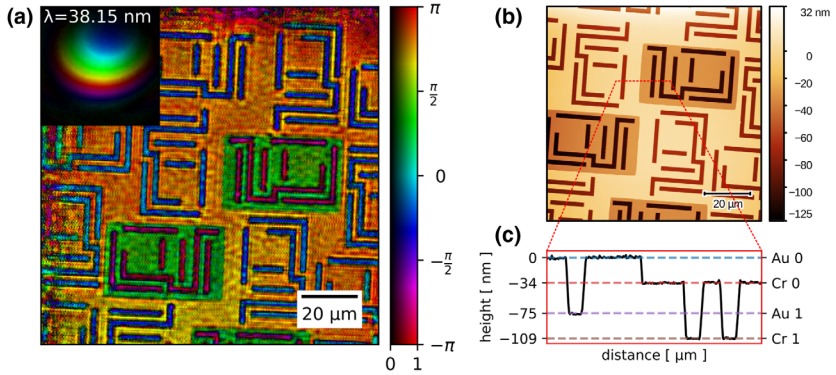

Fig. 2. Imaging of a Cr/Au sample. (a) Ptychography reconstruction for s-polarized measurement at 51° angle of incidence. (b) AFM height measurement capturing the same field of view as the ptychography measurement in (a). Four plateaus of constant height are found, which correspond to two elements that each have structures etched at two discrete depths. (c) AFM height profile along the cross-section indicated in (b).

$r_{s,p}$ at the interface between vacuum and a material with complex refractive index $\mathbf{n}$ are given by the Fresnel equations:

$$r_s = \frac{\cos\theta_1 - \mathbf{n}\cos\theta_2}{\cos\theta_1 + \mathbf{n}\cos\theta_2}, \tag{1a}$$

$$r_p = \frac{\cos\theta_2 - \mathbf{n}\cos\theta_1}{\cos\theta_2 + \mathbf{n}\cos\theta_1}, \tag{1b}$$

where θ_1 and θ_2 refer to the angle of incidence in vacuum and the refracted angle in the material measured from normal, respectively. The angles θ_1 and θ_2 are coupled by Snell's law: $\sin\theta_1 = \mathbf{n}\sin\theta_2$. In the basic form of ellipsometry, the amplitude ratio and phase shift between orthogonally polarized reflections are measured at a single point on the sample to determine the complex-valued refractive index $\mathbf{n}$. Such a calculation is not directly possible using ptychography data, due to the relatively large uncertainty in amplitudes and the inability to compare phases between separate object measurements. Instead, we use the fact that the amplitude and phase variations within a single image are quantitatively accurate, and design an alternative reconstruction procedure that makes effective use of this property. Furthermore, since the illumination intensity of two consecutive ptychography scans should remain constant when the beam is linearly polarized (s or p), we calibrate the probes of both reconstructions in the experiment and adjust the probe amplitudes in the reconstruction to have identical flux ($\sum|P_p|^2 = \sum|P_s|^2$). Based on these considerations, we can define a forward model based on the following four functions that relate the reflectivities defined in Eq. (1) at two spatially separated positions within a single image of an object having different material properties:

$$f_1(\mathbf{n}_1) = \left|\frac{r_s(\mathbf{n}_1)}{r_p(\mathbf{n}_1)}\right|, \tag{2a}$$

$$f_2(\mathbf{n}_2) = \left|\frac{r_s(\mathbf{n}_2)}{r_p(\mathbf{n}_2)}\right|, \tag{2b}$$

$$f_3(\mathbf{n}_1, \mathbf{n}_2, h) = \frac{r_s(\mathbf{n}_1)}{r_s(\mathbf{n}_2)} e^{i\Delta\phi_h}, \tag{2c}$$

$$f_4(\mathbf{n}_1, \mathbf{n}_2, h) = \frac{r_p(\mathbf{n}_1)}{r_p(\mathbf{n}_2)} e^{i\Delta\phi_h}. \tag{2d}$$

Here, $\mathbf{n}_1$ and $\mathbf{n}_2$ are the complex refractive indices of the materials at the different positions, and the phase shift $\Delta\phi = \frac{4\pi}{\lambda} h\cos\theta$ encodes a possible geometrical height difference (see Supplement 1, Section 5). We can connect this model to a set of quantities that can be accurately derived from two ptychography datasets recorded for s- and p-polarization at a single angle:

$$D_1 = \left|\frac{O_s(\mathbf{m}_1)}{O_p(\mathbf{m}_1)}\right|, D_2 = \left|\frac{O_s(\mathbf{m}_2)}{O_p(\mathbf{m}_2)}\right|, D_3 = \frac{O_s(\mathbf{m}_1)}{O_s(\mathbf{m}_2)}, D_4 = \frac{O_p(\mathbf{m}_1)}{O_p(\mathbf{m}_2)}. \tag{3}$$

The coordinates $\mathbf{m}_1$ and $\mathbf{m}_2$ refer to spatially separated pixel coordinates where $\mathbf{n}_1$ and $\mathbf{n}_2$ are present. The first two ratios D_1 and D_2 describe the change of reflectivity when altering the polarization. As D_1 and D_2 are derived from two independent ptychography reconstructions, only the absolute values are well defined. The latter two ratios D_3 and D_4 are complex-valued and compare the reflectivity at $\mathbf{m}_1$ with the reflectivity at $\mathbf{m}_2$. Both D_3 and D_4 are evaluated within the same reconstruction. Therefore, global phase offsets are identical and cancel out.

The values D_{1-4} directly relate to the functions in Eq. (2) and provide six measurements for five unknowns to enable unique determination of $\mathbf{n}_1$, $\mathbf{n}_2$, and h. As directly inverting the forward model is not possible due to its non-convexity, we define a differentiable loss function to retrieve these quantities iteratively,

$$L_\theta(\mathbf{n}_1, \mathbf{n}_2, h) = \sum_{i=1}^{4}\left(|D_i - f_i(\mathbf{n}_1, \mathbf{n}_2, h)| + \left|\frac{1}{D_i} - \frac{1}{f_i(\mathbf{n}_1, \mathbf{n}_2, h)}\right|\right). \tag{4}$$

The loss function consists of both the ratios D_i and its reciprocal $1/D_i$, which makes it symmetric with respect to the order of the two clusters and polarizations, removing any bias. We minimize this loss function with respect to $\mathbf{n}_1$, $\mathbf{n}_2$, and h via an automatic-differentiation-based gradient descent algorithm [43]. While data at a single angle are in principle sufficient, the reconstruction can be improved in accuracy and robustness by using data recorded at multiple incident angles. For such combined reconstructions, we define a new loss function $L_{\text{total}} = \frac{1}{N_\theta}\sum_i^{N_\theta} L_{\theta_i}$, being the average of the loss functions at different angles. In this way, spatially resolved maps of complex refractive indices and height variations can be reconstructed by pairwise comparison of different positions within the ptychography images. It should be noted that our approach is tailored to objects that exhibit spatial variations of the refractive index, i.e., containing two or more materials, to ensure that Eqs. (2) and (3) contain sufficient independent measurements. But this is not a significant constraint, as there would

not be a need for imaging ellipsometry if a sample does not contain such spatial structure.

B. Clustering on Complex Values

While our ptychographic imaging ellipsometry concept in principle works with the data from single pixels at coordinates $\mathbf{m_1}$ and $\mathbf{m_2}$ as input for Eq. (3), realistic samples contain a limited amount of materials. Especially lithographic nanostructures as found in the semiconductor industry typically consist of structured stratified layers made from different elements. Therefore, using clustering in the analysis is a natural analytical step to identify and group areas with constant optical properties.

We apply k-means clustering [46] on a dataset comprising ptychography reconstructions from 5 different angles in the range $51° \leq \theta \leq 57°$ illuminated with both s- and p-polarized EUV light at $\lambda = 38$ nm. The range of angles is selected based on the contrast within the measured diffraction patterns, overall reflected flux, and the tilt-induced deformation of the diffraction patterns.

Performing measurements at more grazing angles ($\theta > 57°$) leads to a loss of contrast between the 0^{th} and higher orders in the diffraction pattern. This is caused by height steps within the sample that average around 75 nm, resulting in a 2π-shift close to $\theta \approx 59°$. On the other hand, measuring at more oblique incidence $\theta < 51°$ results in low flux and thus long measurement times (≈ 2 h). Each measurement is reconstructed individually, leaving us with relative reflectivities per angle and polarization state.

The result of the clustering analysis is shown in Fig. 3(a). In the analysis, we use the real and imaginary part of the reconstructions at each illumination angle and polarization state, which yields 20 independent data elements per pixel. The clustering algorithm clearly identifies four areas that correspond to the Cr- and Au-layers, each having two distinct height steps. The analysis assigns a fifth cluster to the edges of the spatial features, with a width of approximately the resolution limit of the image, where the amplitude and phase are less well defined. These clusters match the different areas observed in the individual ptychography reconstructions and AFM data from Figs. 2(a), 2(b).

C. Retrieving Complex Refractive Indices of Clusters

As mentioned previously, in principle it is possible to find a unique solution for $\mathbf{n}_1$, $\mathbf{n}_2$, and h from data at a single angle, as there are as many unknown parameters to solve as independent constraints in the loss function. However, the height step induces a phase shift of $\Delta\phi = \frac{4\pi}{\lambda} h \cos\theta$, which may lead to phase wrapping ($\Delta\phi > 2\pi$) for larger heights and steeper incidence angles. Such phase ambiguities are resolved by combining measurements at multiple incidence angles, since each angle has a different relation between phase and height. As discussed above, we generally perform reconstructions based on multi-angle data to improve accuracy, using the combined loss function that averages over multi-angle datasets. Gradient descent optimization with this loss function is sensitive to the phase shifts between different angles. As a result, this optimization has a well-defined global minimum within a larger height range (Supplement 1, Fig. S13).

Starting out from the clustered images as shown in Fig. 3(a) allows reconstruction of n, k, and h based on the amplitude and phase values from each cluster C_i as the input to the model. To evaluate ratios D_{1-4} from Eq. (3) for each cluster, we define $O_{s,p}(C_i) := \langle O_{s,p}(\mathbf{m})\rangle_{\mathbf{m}\in C_i}$. The optimization procedure then yields refractive indices of $\mathbf{n}_{\text{Au}} = (0.86 \pm 0.01) + (0.54 \pm 0.02)i$ and $\mathbf{n}_{\text{Cr}} = (0.82 \pm 0.01) + (0.24 \pm 0.01)i$, which are in good agreement with literature values ($\mathbf{n}^{\text{lit}}_{\text{Au}} = 0.81 + 0.40i$ [47], $\mathbf{n}^{\text{lit}}_{\text{Cr}} = 0.81 + 0.15i$ [48]). The uncertainties are evaluated via the standard deviation after convergence, starting from 2000 initial guesses. The starting values are drawn from a uniform distribution ranging from $\mathbf{n}_{\text{Au}}, \mathbf{n}_{\text{Cr}} \in \mathcal{U}[0.25, 0.75] + \mathcal{U}[0.25, 0.75]i$ and $h \in \mathcal{U}[-35, -29]$ nm. Despite the variation in starting guesses, all values converging to a small standard deviation indicate robustness against local minima and hence a suitable choice of loss function. Their distributions after 10^4 iterations are shown in Figs. 3(b)–3(c). In parallel, we recover the height step between the gold and chromium layers $h_{\text{Au-Cr}} = -34.5(1.1)$ nm. Compared to literature values for bulk materials, we find a small overestimation of the imaginary part for both materials. While the error bar on the literature values may also be significant, a possible cause for this discrepancy is the fact that we measure on thin films, which may contain grain structure that induces additional scattering losses.

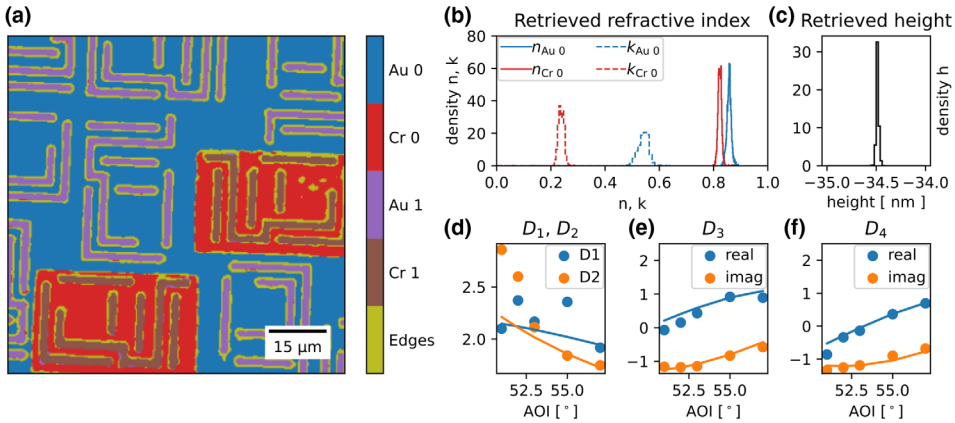

Fig. 3. Clustering and retrieval of refractive indices for two clusters. (a) The combined reconstructions assigned to their k-means clusters (here: $k = 5$). All 5 illumination angles and both s- and p-polarization measurements were used for clustering. The first four clusters correspond to the material and height steps in the samples, whereas the last cluster ("Edges," yellow) represents edges. Edges show artifacts due to reflection geometry and misalignment of the individual reconstructions. The refractive indices and relative height step between clusters "Au 0" and "Cr 0" are retrieved by fitting to their complex ratios. (b, c) Distributions (normalized density plots) of retrieved complex refractive indices and height step between both clusters, using different initial values. (d–) Averaged ratios D_{1-4} of the two clusters "Au 0" and "Cr 0." The lines plotted correspond to the fit given the retrieved complex refractive indices.

In Figs. 3(d)–3(f), the complex ratios are shown for $D_{1,2}$, D_3, and D_4, respectively. Note that D_3 and D_4 are complex-valued. Hence, their real and imaginary parts are plotted separately. The accurate fit for D_3 and D_4 compared to D_1 and D_2 highlights the importance of quantitative phase retrieval at both polarization states from single images. The reciprocals of the ratios, which are required for evaluating the loss function from Eq. (4), are shown in Supplement 1, Fig. S11.

D. High-Resolution Mapping of Optical Properties

While the analysis based on k-means clustering is quite generally applicable for analyzing nanostructured surfaces, in principle our ptychographic ellipsometry approach can be applied to the reconstructed images on a pixel-by-pixel basis as well, to provide high-resolution spatial maps of the optical properties and height variations. The approach is mostly identical, retrieving the complex ratios D_1 to D_4 in Eq. (3) by comparing different pixels within an image. However, since the signal from a single pixel is typically less accurate than for a clustered area, the choice of a reference position will influence the retrieved values more significantly. As a reference for the retrieval of n, k, h, we took the mean amplitude and phase values from the pixels included in the gold surface cluster Au 0. In Supplement 1, Fig. S10, we show the resulting maps of the D parameters from Eq. (3) that serve as the input for the retrieval. By performing such a reconstruction where we optimize the loss function on each pixel, we obtain maps of n, k, and h as shown in Figs. 4(a)–4(c). Since the real part of the refractive indices for gold and chromium from literature are close ($n^{\mathrm{lit}}_{\mathrm{Au}} \approx n^{\mathrm{lit}}_{\mathrm{Cr}} = 0.81$), a homogeneous real part of the refractive index map is expected in Fig. 4(a). On the other hand, the imaginary part in Fig. 4(b) shows a clear distinction between different materials, with the rectangular chromium patterns being clearly visible. However, both the real and imaginary parts still resemble spatial structures where only a height step is present, but the material is not changing. The retrieved height map in Fig. 4(c) shows four distinct height steps that correspond to the different materials, similar to the AFM measurement in Fig. 2(b).

As the sample consists only of a discrete set of elements and height steps, and the parameter retrieval is performed independently for all pixels, the variation in the final results is a measure of the accuracy of the retrieved quantities. In Fig. 4(d), we show the distributions, plotted for each cluster individually. For both elements, we find a broadening for clusters assigned to the grooves of the sample. More clearly separated are the retrieved heights for different clusters. With an increasing distance from the reference plane ($h = 0$ nm) and a simultaneously decreasing feature size, the distribution is broadened, similar to the observations for the refractive indices. The reason for this behavior is readily understood when looking at the minimization landscape (Supplement 1, Fig. S13), showing regular and deep local minima at heights corresponding to 2π phase steps in the optical path length. While the angular diversity in the dataset ensures that the correct minimum is uniquely defined, the experimentally accessible scan range could be increased for more robust convergence. The mean and standard deviation are summarized in Table 1.

To assess the accuracy of the ptychography reconstructions and their influence on the refractive index retrieval, we repeated this analysis using data from single angles. For the images with the highest signal-to-noise ratios (angle of incidence 51°, 52°, and 53°), the resulting refractive index values are consistent

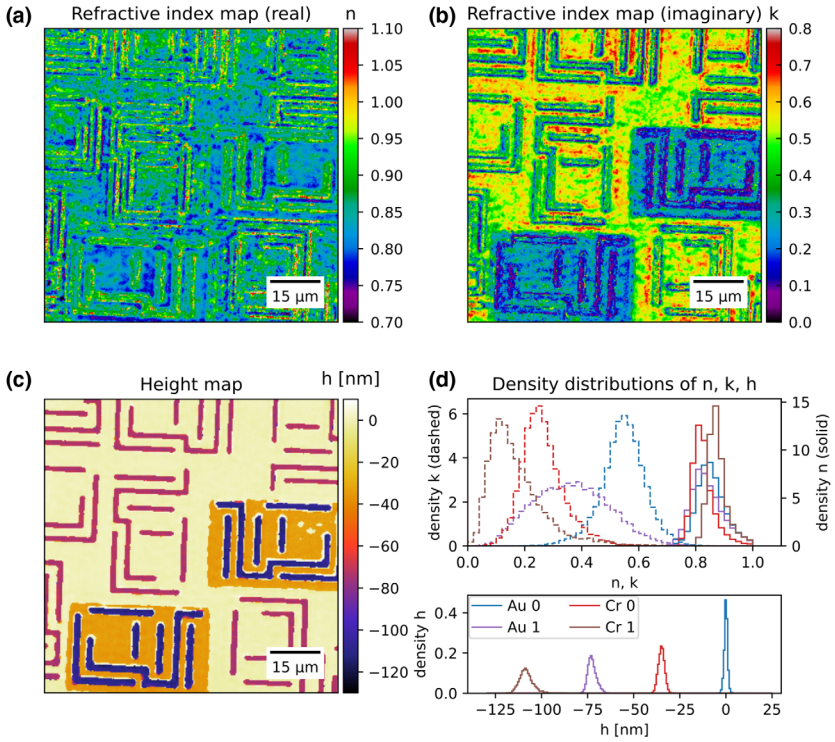

Fig. 4. High-resolution spatial maps of retrieved the optical properties. (a, b) Real and imaginary parts of the reconstructed refractive indices. (c) Reconstructed height map of the sample. To reconstruct the maps in (a,b,c), the ratios of all pixels were evaluated with respect to the complex reflectivities averaged in a clustered region of "Au 0." For that purpose, the complex reflective index in that region retrieved in the cluster analysis was used as a reference. (d) Top: distribution of spatially varying of the real and imaginary parts from (a) and (b), plotted as solid and dashed lines, respectively. Bottom: distribution of spatially varying reconstructed height map. In both cases, the distributions are normalized density plots categorized per cluster.

Table 1. Mean and Standard Deviation for *n*, *k*, and *h* Using Distributions from Fig. 4(d)

Cluster	n	k	h [nm]
Au 0	0.86 ± 0.06	0.55 ± 0.08	-0 ± 1
Au 1	0.85 ± 0.06	0.36 ± 0.13	-72 ± 2
Cr 0	0.83 ± 0.04	0.26 ± 0.07	-35 ± 2
Cr 1	0.88 ± 0.06	0.17 ± 0.10	-108 ± 4

with the values in Table 1, with an increase in error bars between 20%–100%. The error increases further for the datasets taken at higher angles, due to the lower contrast in the diffraction patterns in that range. This analysis shows that independent ptychography measurements provide consistent results, and indicate that the accuracy of the refractive index reconstructions is mainly determined by signal-to-noise ratio and statistics.

Our measurements were performed with a detection numerical aperture (NA) of 0.063, which results in a diffraction limit of 300 nm. Knife-edge analysis of our retrieved ptychography images indicates that we indeed achieve such a resolution. While there is still significant room for improvement by implementing higher-NA EUV detection [17,32,33], the current resolution already goes well beyond state-of-the-art optical imaging ellipsometers [25–27], while maintaining the advantages of low-NA analysis where averaging over angular ranges is limited.

4. DISCUSSION AND CONCLUSION

Our results show that our ptychography-based approach to ellipsometric EUV imaging provides quantitatively accurate, high-resolution structural information about complex nanostructured samples. The phase and amplitude information obtained from consecutive ptychography scans at s- and p-polarization is found to be sufficiently accurate to serve as the basis for further quantitative analysis. The main advantage of ptychographic imaging is the reconstruction of accurate complex field information. This feature enables a reconstruction approach based on ratios of complex fields at different object positions $D_{3,4}$ in Eq. (3)], which we find to be a powerful constraint in retrieving the optical properties of the object. Especially in the EUV range, where both phase-sensitive measurements and high-resolution imaging are particularly challenging, our approach provides a significant advantage.

Our reconstruction approach is based on iterative optimization using a differentiable forward model, which in the present study consisted of the Fresnel equations for surface reflections combined with spatial height variations. However, the model can be adapted and/or extended to include other material properties that influence the reflected field. Therefore, the present study provides a template for other forms of quantitative imaging, potentially also including functional properties if the time resolution of the measurement is sufficient. While we use EUV light (38 nm) for high transverse and height resolution and element contrast, ptychographic imaging ellipsometry should in principle work with any coherent light source.

The nonlinearity of high-harmonic generation increases the experimental complexity, as intensity fluctuations, beam drift, and decoherence in combination with long exposure times, lead to deviations from the ideal diffraction patterns. Furthermore, the set of multilayer mirrors that we used to select a single harmonic wavelength around 38 nm still has finite reflectance for adjacent harmonics (see Supplement 1, Section 3), which in principle should be included as additional probe modes at different wavelengths in the diffraction patterns. Attempts to perform such multi-wavelength reconstructions failed to converge, most likely due to the relatively low flux of the remaining harmonics, and the strong dispersion of the sample. While that observation means that the weak signal in these background harmonics does not significantly influence the retrieved object field at the main harmonic when performing single-mode reconstructions, it is a probable reason for the appearance of speckles in the reconstructed object images. Such speckles are apparent when comparing the ptychography reconstruction in Fig. 2(a) with the AFM height map shown in Fig. 2(b). Although individual ptychographic reconstructions [Fig. 2(a)] exhibit speckle-like artifacts due to partial coherence and residual background contributions, these artifacts vary with illumination angle and polarization and therefore do not form consistent features across the full multi-angle, multi-polarization dataset. Therefore, such artifacts in individual reconstructions did not influence the final map of complex refractive indices and height data.

The retrieved height values (see Table 1) are in good agreement with independent measurements using AFM. An even higher accuracy can be reached if the reconstruction is limited to height steps only, keeping the refractive indices fixed. As the comparison between different materials involves the determination of multiple parameters, the accuracy of each individual parameter is naturally lower compared to a single-parameter fit.

Our analysis does not explicitly include surface roughness, as the lithographically produced samples had very smooth surfaces. From AFM analysis, we estimate the rms roughness to be around 1 nm for both the Cr- and Au-coated areas, which would result in a negligible contribution to the Fresnel equations based on an estimate of the Debye–Waller factors [7]. To still investigate the potential influence, we have performed an extended analysis including such roughness effects (see Supplement 1, Section 9). This analysis indeed showed a minor effect, within the error margins of the measurement. However, inhomogeneities in the deposited thin film structures could lead to scattering losses that lead to an overestimation of the *k*-values compared to literature values for bulk media. Furthermore, the results could also be influenced by the oxidation of the Cr, although such a film would have a thickness on the order of a Nanometer as Cr oxidation results in a passivating layer. Another potential systematic error is the accuracy with which the incident angle is determined, which can affect both reconstruction quality and height estimates. Tests with reconstructions at slightly different angles show that these effects are insignificant for our experimental parameters and angular accuracy. As each dataset consists of multiple independent image reconstructions, accurate co-registration of these images is an important aspect for the parameter estimation. Currently, this is achieved by overlapping edges, which is wellsuited for samples that contain sharp edges. Any misalignment would mainly affect the retrieved material properties at those edges, effectively reducing the spatial resolution.

Overall, we conclude that our ptychography-based approach to imaging ellipsometry is flexible and yields accurate results. It enables quantitative imaging in spectral ranges that are challenging in terms of optics, such as the extreme ultraviolet. As a next step, the method can be extended to more complex structures, including partially transparent layers and larger amounts of elements.

Interestingly, the presence of more materials adds more independent equations than unknowns, which could lead to a more robust reconstruction. However, an increased number of clusters would of course also affect the statistics per cluster, so a decisive statement on performance and accuracy for such structures requires a more in-depth analysis. These aspects will be addressed in future work.

Funding. European Research Council (864016); Dutch Research Council.

Acknowledgment. We thank Matthijs Velsink and Mengqi Du for insightful discussions. We acknowledge the support from the European Research Council (ERC-CoG 864016, project 3D-VIEW). This work was conducted at the Advanced Research Center for Nanolithography, a public-private partnership between the University of Amsterdam (UvA), Vrije Universiteit Amsterdam (VU), Rijksuniversiteit Groningen (RUG), the Dutch Research Council (NWO), and the semiconductor equipment manufacturer ASML.

Disclosures. The authors declare no conflicts of interest.

Data availability. All data supporting the findings of this study are available from the corresponding author upon reasonable request.

Supplemental document. See Supplement 1 for supporting content.

REFERENCES

1. M. Fricker, J. Runions, and I. Moore, "Quantitative fluorescence microscopy: from art to science," Annu. Rev. Plant Biol. **57**, 79–107 (2006).
2. Y. Park, C. Depeursinge, and G. Popescu, "Quantitative phase imaging in biomedicine," Nat. Photonics **12**, 578–589 (2018).
3. M. A. Tschudin, D. A. Broadway, P. Siegwolf, *et al.*, "Imaging nanomagnetism and magnetic phase transitions in atomically thin CrSBr," Nat. Commun. **15**, 6005 (2024).
4. R. M. A. Azzam, N. M. Bashara, and S. S. Ballard, "Ellipsometry and polarized light," Phys. Today **31**, 72 (1978).
5. H. G. Tompkins and E. A. Irene, eds. *Handbook of Ellipsometry* (William Andrew Publishing, 2005).
6. C. Tarrio, R. N. Watts, T. B. Lucatorto, *et al.*, "Optical constants of in situ-deposited films of important extreme-ultraviolet multilayer mirror materials," Appl. Opt. **37**, 4100–4104 (1998).
7. D. L. Windt, W. C. Cash, M. Scott, *et al.*, "Optical constants for thin films of C, diamond, Al, Si, and CVD SiC from 24 Å to 1216 Å," Appl. Opt. **27**, 279 –295 (1988).
8. H. F. Hazebroek and A. A. Holscher, "Interferometric ellipsometry," J. Phys. E: Sci. Instrum. **6**, 822–826 (1973).
9. L. R. Watkins, "Interferometric ellipsometer," Appl. Opt. **47**, 2998–3001 (2008).
10. C.-h. Lin, C. Chou, and K.-s. Chang, "Real time interferometric ellipsometry with optical heterodyne and phase lock-in techniques," Appl. Opt. **29**, 5159 –5162 (1990).
11. C. Chou, H.-K. Teng, C.-C. Tsai, *et al.*, "Balanced detector interferometric ellipsometer," J. Opt. Soc. Am. A **23**, 2871–2879 (2006).
12. V. Soltwisch, A. Fischer, C. Laubis, *et al.*, "Polarization resolved measurements with the new EUV ellipsometer of PTB," Proc. SPIE **9422**, 942213 (2015).
13. M. Yamamoto and M. Furudate, "Ellipsometry in the extreme ultraviolet region with multilayer polarizers," Thin Solid Films **313–314**, 751–755 (1998).
14. C. Porter, T. Coenen, N. Geypen, *et al.*, "Soft X-ray: novel metrology for 3D profilometry and device pitch overlay," Proc. SPIE **12496**, 124961I (2023).
15. M. Tanksalvala, C. L. Porter, Y. Esashi, *et al.*, "Nondestructive, high-resolution, chemically specific 3D nanostructure characterization using phase-sensitive EUV imaging reflectometry," Sci. Adv. **7**, eabd9667 (2021).
16. L. Loetgering, S. Witte, and J. Rothhardt, "Advances in laboratory-scale ptychography using high harmonic sources [Invited]," Opt. Express **30**, 4133–4164 (2022).
17. W. Eschen, L. Loetgering, V. Schuster, *et al.*, "Material-specific high-resolution table-top extreme ultraviolet microscopy," Light. Sci. Appl. **11**, 117 (2022).
18. R. Soufli and E. M. Gullikson, "Reflectance measurements on clean surfaces for the determination of optical constants of silicon in the extreme ultraviolet–soft-X-ray region," Appl. Opt. **36**, 5499–5507 (1997).
19. M. Tryus, S. Herbert, D. Wilson, *et al.*, "Spatially resolved spectroscopic extreme ultraviolet reflectometry for laboratory applications," J. Nanosci. Nanotechnol. **19**, 562–567 (2019).
20. S. Danylyuk, S. Herbert, P. Loosen, *et al.*, "Multi-angle spectroscopic extreme ultraviolet reflectometry for analysis of thin films and interfaces," Phys. Status Solidi C **12**, 318–322 (2015).
21. S. Döring, F. Hertlein, A. Bayer, *et al.*, "EUV reflectometry for thickness and density determination of thin film coatings," Appl. Phys. A **107**, 795–800 (2012).
22. S. N. Jasperson and S. E. Schnatterly, "An improved method for high reflectivity ellipsometry based on a new polarization modulation technique," Rev. Sci. Instrum. **40**, 761–767 (1969).
23. E. Masetti, M. Montecchi, and S. E. Segre, "Proposal for ellipsometer configurations allowing phase-sensitive detection," Appl. Opt. **36**, 8179–8183 (1997).
24. L. Asinovski, D. Beaglehole, and M. T. Clarkson, "Imaging ellipsometry: quantitative analysis," Physica Status Solidi (a) **205**, 764–771 (2008).
25. R. Kenaz and R. Rapaport, "Mapping spectroscopic micro-ellipsometry with sub-5 microns lateral resolution and simultaneous broadband acquisition at multiple angles," Rev. Sci. Instrum. **94**, 023908 (2023).
26. Q. Zhan and J. R. Leger, "Microellipsometer with radial symmetry," Appl. Opt. **41**, 4630–4637 (2002).
27. J. Oh, J. Son, C. Yoon, *et al.*, "Ultra-wide-field imaging Mueller matrix spectroscopic ellipsometry for semiconductor metrology," Nat. Commun. **16**, 8512 (2025).
28. B. Vodungbo, A. B. Sardinha, J. Gautier, *et al.*, "Polarization control of high order harmonics in the EUV photon energy range," Opt. Express **19**, 4346–4356 (2011).
29. P. W. Wachulak, A. Bartnik, and H. Fiedorowicz, "Sub-70 nm resolution tabletop microscopy at 13.8 nm using a compact laser-plasma EUV source," Opt. Letters **35**, 2337–2339 (2010).
30. S. Eisebitt, J. Lüning, W. F. Schlotter, *et al.*, "Lensless imaging of magnetic nanostructures by X-ray spectro-holography," Nature **432**, 885–888 (2004).
31. G. S. M. Jansen, X. Liu, K. S. E. Eikema, *et al.*, "Broadband extreme ultraviolet dispersion measurements using a high-harmonic source," Opt. Lett. **44**, 3625–3628 (2019).
32. D. F. Gardner, M. Tanksalvala, E. R. Shanblatt, *et al.*, "Subwavelength coherent imaging of periodic samples using a 13.5 nm tabletop high-harmonic light source," Nat. Photonics **11**, 259–263 (2017).
33. G. K. Tadesse, W. Eschen, R. Klas, *et al.*, "Wavelength-scale ptychographic coherent diffractive imaging using a high-order harmonic source," Sci. Rep. **9**, 1735 (2019).
34. R. Wang, Q. Zhao, L. Loetgering, *et al.*, "Ptychography at all wavelengths," Nat. Rev. Methods Primers **5**, 68 (2025).
35. T. Aidukas, N. W. Phillips, A. Diaz, *et al.*, "High-performance 4-nm-resolution X-ray tomography using burst ptychography," Nature **632**, 81–88 (2024).
36. A. M. Maiden and J. M. Rodenburg, "An improved ptychographical phase retrieval algorithm for diffractive imaging," Ultramicroscopy **109**, 1256–1262 (2009).
37. P. Thibault, M. Dierolf, A. Menzel, *et al.*, "High-resolution scanning X-ray diffraction microscopy," Science **321**, 379–382 (2008).
38. M. Guizar-Sicairos and P. Thibault, "Ptychography: a solution to the phase problem," Phys. Today **74**, 42–48 (2021).
39. M. D. Seaberg, B. Zhang, D. F. Gardner, *et al.*, "Tabletop nanometer extreme ultraviolet imaging in an extended reflection mode using coherent Fresnel ptychography," Optica **1**, 39–44 (2014).
40. C. L. Porter, M. Tanksalvala, M. Gerrity, *et al.*, "General-purpose, wide field-of-view reflection imaging with a tabletop 13 nm light source," Optica **4**, 1552–1557 (2017).
41. A. De Beurs, L. Loetgering, M. Herczog, *et al.*, "aPIE: an angle calibration algorithm for reflection ptychography," Opt. Lett. **47**, 1949–1952 (2022).
42. E. R. Shanblatt, C. L. Porter, D. F. Gardner, *et al.*, "Quantitative chemically specific coherent diffractive imaging of reactions at buried interfaces with few nanometer precision," Nano Lett. **16**, 5444–5450 (2016).

43. A. Pazke, S. Gross, S. Chintala, *et al.*, "Automatic differentiation in PyTorch," in *31st Conference on Neural Information Processing Systems (NIPS 2017)*, (Long Beach, California, USA, 2017).
44. F. Zhang, A. Pelekanidis, A. Karpavicius, *et al.*, "Characterizing post-compression of mJ-level ultrafast pulses via loose focusing in a gas cell," Opt. Express **32**, 40990–41003 (2024).
45. W. Becker, A. Lohr, M. Kleber, *et al.*, "A unified theory of high-harmonic generation: application to polarization properties of the harmonics," Phys. Rev. A **56**, 645–656 (1997).
46. J. MacQueen, "Some methods for classification and analysis of multivariate observations," in *Proceedings of the Fifth Berkeley Symposium on Mathematical Statistics and Probability, Volume 1: Statistics* (University of California Press, 1967), Vol. **5.1**, pp. 281–298.
47. W. S. Werner, K. Glantschnig, and C. Ambrosch-Draxl, "Optical constants and inelastic electron-scattering data for 17 elemental metals," J. Phys. Chem. Ref. Data **38**, 1013–1092 (2009).
48. B. L. Henke, E. M. Gullikson, and J. C. Davis, "X-ray interactions: photoabsorption, scattering, transmission, and reflection at e = 50–30,000 eV, z = 1–92," At. Data Nuclear Data Tables **54**, 181–342 (1993).